



Optimal sound-absorbing structures†

Min Yang, ^a Shuyu Chen,^b Caixing Fu^{ab} and Ping Sheng ^{*ac}

Cite this: *Mater. Horiz.*, 2017, 4, 673

Received 1st March 2017,
Accepted 15th May 2017

DOI: 10.1039/c7mh00129k

rsc.li/materials-horizons

The causal nature of the acoustic response dictates an inequality that relates the two most important aspects of sound absorption: the absorption spectrum and the sample thickness. We use the causality constraint to delineate what is ultimately possible for sound absorbing structures, and denote those which can attain near-equality for the causality constraint to be “optimal.” Anchored by the causality relation, a design strategy is presented for realizing structures with target-set absorption spectra and a sample thickness close to the minimum value as dictated by causality. By using this approach, we have realized a 10.86 cm-thick structure that exhibits a broadband, near-perfect flat absorption spectrum starting at around 400 Hz, while the minimum sample thickness from the causality constraint is 10.36 cm. To illustrate the versatility of the approach, two additional optimal structures with different target absorption spectra are presented. This “absorption by design” strategy would enable the tailoring of customized solutions to difficult room acoustic and noise remediation problems.

Sound absorption is important for room acoustics and remediation of noise that can arise from machines, rail cars, or cooling fans of computer server arrays in search engines or cloud computing. The traditional means of acoustic absorption, such as porous and fibrous,^{1–3} or gradient index materials,⁴ can be either bulky or structurally weak. Micro-perforated panels (MPP) with a tuned cavity depth behind the panels are effective for indoor sound absorption within a certain frequency range,^{5–7} but are not broadly applicable. During the past decade, locally resonant artificial structures,^{8–14} acoustic metamaterials,^{15,16} and metasurfaces^{17,18} have shown diverse functionalities in the manipulation of sound such as negative refraction,^{19–21} subwavelength imaging,^{22–24} cloaking,^{25,26} one-way transmittance,^{27,28} and

Conceptual insights

Conventional sound absorbing materials have fixed absorption spectra which can only be adjusted by varying the sample thickness. The effective absorbers for low frequency sound are usually bulky. In recent years acoustic metamaterials have diversified the functionalities of sound manipulation, including sound absorption. However, they are inherently constrained by the narrow frequency band character and hence are somewhat limited in their usefulness. It would therefore be most desirable if a sound absorber can be designed to fit the noise spectrum, with the minimum allowed thickness. Such sound absorbing structures can now be realized through a design recipe that incorporates the causality constraint on the acoustic response. The strategy involves the use of acoustic metamaterials with multiple resonances at calculated frequencies to attain the target absorption spectrum. A crucial parameter of the design is then fixed by requiring the resonance mode density to satisfy the causality constraint, in the form of a minimum sample thickness requirement. In this work we demonstrate this sound absorber design strategy by implementing three examples. In all cases the absorption performance in the target frequency range is without peer, with a sample thickness that is guaranteed to be the minimum allowed by the law of nature.

even highly efficient sound absorption within a compact volume.^{29–43} However, due to the dispersive nature of the resonances, these applications are generally narrowband in character. It is thus reasonable to ask whether there is a way to define the “best” absorber performance and its associated limitations. In particular, the question regarding the limiting minimum thickness for a given absorption performance would be of special interest, since in the absence of the thickness consideration the problem of sound absorption becomes trivial. Defining the limit can inform us of the potential that may still exist for better absorption performance, so as to induce efforts for improvement.

Causal optimality in sound absorption

Material response functions for the electromagnetic and acoustic waves must satisfy the causality principle.⁴⁴ For the electromagnetic waves, the causal nature of the material response function was found to result in an inequality that relates a given

^a Department of Physics, HKUST, Clear Water Bay, Kowloon, Hong Kong, China.
E-mail: sheng@ust.hk

^b Acoustic Metamaterials Co. Ltd, No. 2 Science Park West Avenue, Hong Kong Science Park, Shatin, New Territories, Hong Kong, China

^c Institute for Advanced Study, HKUST, Clear Water Bay, Kowloon, Hong Kong, China

† Electronic supplementary information (ESI) available. See DOI: 10.1039/c7mh00129k

absorption spectrum to the sample thickness.^{45,46} Adapted to acoustics, this relation (for sound waves propagating in air) can be expressed in the following form for a flat absorbing material (or a structure) with thickness d sitting on a reflecting substrate:

$$d \geq \frac{1}{4\pi^2} \frac{B_{\text{eff}}}{B_0} \left| \int_0^\infty \ln[1 - A(\lambda)] d\lambda \right| = d_{\text{min}}, \quad (1)$$

where λ denotes the sound wavelength in air, $A(\lambda)$ is the absorption coefficient, B_{eff} denotes the effective bulk modulus of the sound absorbing structure in the static limit, and B_0 is the bulk modulus of air. A detailed derivation of eqn (1) is given in the ESI.† We define a sound absorbing structure to be optimal if equality or near-equality can be attained in the above relation. Some obvious implications immediately follow from eqn (1). For example, the total absorption within a finite frequency range is not possible for any sample of finite thickness. Also, high absorption at low frequencies would dominate the contribution to sample thickness. However, $A(\lambda) \sim 1$ at a low frequency is entirely possible for a subwavelength sample thickness,^{30,31} provided the absorption peak is narrow.

In the limit of equality, eqn (1) can be satisfied with tradeoffs between three parameters: the sample thickness, frequency bandwidth, and the magnitude of the absorption coefficient within the frequency band. By specifying two out of three parameters, the other one can be optimized. Here we present a design strategy that can realize the target $A(\lambda)$ spectrum with the minimum required sample thickness. In particular, a sound absorbing structure is presented that can achieve a flat, near-perfect absorption spectrum starting at 400 Hz. While the actual sample thickness is 10.86 cm, the right-hand side of eqn (1) is shown to yield 10.55 cm. In the ESI,† we show that a similar optimal sample, with $d = 5.93$ cm, can display the same flat, near-perfect absorption spectrum above 752 Hz. A third optimal sample is shown to reproduce a rather artificial made-up target $A(\lambda)$ that has a “notch” in the middle of a near-perfect flat absorption spectrum; it can thereby selectively reflect sound within a certain frequency range. In all the designs the causal optimality is built-in, as the means to determine a crucial geometric parameter.

Strategy for absorption by design

Consider a designed acoustic metamaterial, with N resonances, that are constrained by an overall objective $A(\lambda)$ that is related to the target sample impedance Z by the relation $A = 1 - |(Z/Z_0 - 1)/(Z/Z_0 + 1)|^2$. The overall impedance of the metamaterial can be expressed as^{30,47}

$$Z = i \frac{Z_0 d}{\omega v_0} \left[\sum_n^N \frac{\alpha_n}{\Omega_n^2 - \omega^2 - i\beta\omega} \right]^{-1}, \quad (2)$$

where $Z \equiv p/v$ denotes the surface impedance, p being the sound pressure modulation and v the displacement velocity in response to the pressure at the surface of the metamaterial, $v_0 = 343 \text{ m s}^{-1}$ is the speed of sound in air, $Z_0 = \rho_0 v_0$ is the air impedance, ρ_0 being the air density, ω is the angular frequency,

Ω_n denotes the n th resonance frequency, and $\beta \ll \omega$ describes the weak system dissipation for the acoustic metamaterial. In this work, we choose Fabry–Pérot (FP) resonators for realizing the acoustic metamaterial structure, and in that case the dimensionless oscillator strength $\alpha_n = 4d\phi\Omega_n/(\pi v_0 N)$ for the 1st order FP resonances, which will be used for the design strategy presented below. Here the parameter ϕ is the ratio of the surface area occupied by FP channels' cross sections to the total surface area exposed to sounds. It is a geometric measure of the resonant channels' coupling to the incident sound. As can be seen below, the parameter ϕ ties together the causality constraint with the sample design parameters. Also, from the ESI† it can be shown that $B_{\text{eff}} = B_0/\phi$. It should be noted that for eqn (2) to be an accurate description, the lateral size of the metamaterials' unit must be very subwavelength in scale so that the diffraction effects can be neglected. This is indeed a reasonable approximation in the present work.

In the idealized case where we have a large N so that the summation in eqn (2) can be approximated by an integral with $\Omega_N \rightarrow \infty$, the summation in eqn (2) can be replaced by integration:

$$Z(\omega) \simeq i \lim_{\beta \rightarrow 0} \frac{Z_0 d}{\omega v_0} \left[\int_0^\infty \frac{\alpha(\Omega) D(\Omega)}{\Omega^2 - \omega^2 - i\beta\omega} d\Omega \right]^{-1}, \quad (3a)$$

where $D(\Omega)$ denotes the mode density per unit frequency; it is an important function that must be determined in accordance with the target absorption spectrum. In eqn (3), the imaginary part of the impedance is generally negligible, owing to the oscillatory nature of the real part of the integrand in the square bracket. In the limit of $\beta \rightarrow 0$, the imaginary part of the integrand is accurately a delta function, hence we have

$$Z(\omega) \simeq \frac{Z_0 d}{\pi \omega v_0} \left[\int_0^\infty \alpha(\Omega) D(\Omega) \delta(\omega^2 - \Omega^2) d\Omega \right]^{-1} = \frac{2Z_0 d}{\pi v_0} [\alpha(\omega) D(\omega)]^{-1}. \quad (3b)$$

By definition we have $D(\Omega) = \Delta n/\Delta\Omega$, hence from eqn (3b) $\Delta\Omega/\Delta n = \pi v_0 \alpha(\Omega) Z(\Omega)/(2Z_0 d)$. As $\alpha(\Omega) = 4d\phi\Omega/(N\pi v_0)$, it follows that $\Delta\Omega/\Delta n = (2\phi\Omega/N)[Z(\Omega)/Z_0]$. By allowing $\Delta n/N \rightarrow d\bar{n}$ in the limit of $N \rightarrow \infty$, with $\bar{n} = (n - 1)/N$, we have

$$\frac{d\Omega}{d\bar{n}} = 2\phi \left[\frac{Z(\Omega)}{Z_0} \right] \Omega, \quad (4)$$

where \bar{n} is treated as a continuous variable. Eqn (4) relates the necessary mode distribution to the target impedance. Below we specialize to the example of a broadband absorber for illustrating the design strategy. In that case we want to have a flat $Z = Z_0$ when $\Omega > \Omega_c$ and $Z_0/Z = 0$ when $\Omega < \Omega_c$. Eqn (4) can be solved under the initial condition of $\Omega = \Omega_c$ at $\bar{n} = 0$, so that $\Omega_{\bar{n}} = \Omega_c \exp[2\phi\bar{n}]$. It can be easily seen that $\alpha(\Omega)D(\Omega) = 2d/(\pi v_0)$ is a constant for $\Omega > \Omega_c$, and the integral in eqn (3) can be obtained to yield

$$\frac{Z}{Z_0} = \frac{\pi}{\pi - 2i \tanh^{-1}(\Omega_c/\omega)}. \quad (5)$$

The behavior for the real and imaginary parts of Z is shown in Fig. 1a. The imaginary part, owing to the oscillatory nature of

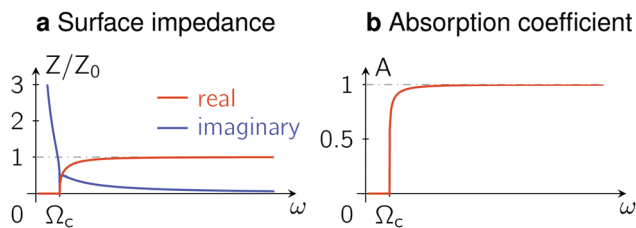


Fig. 1 Broadband sound absorption and the optimally designed surface impedance. Here we consider an idealized acoustic metamaterial with continuously distributed resonance frequencies above a cutoff Ω_c . If the density of the mode $D(\Omega)$ satisfies $\alpha(\Omega)D(\Omega) = 2d/(\pi v_0)$ with $\alpha(\Omega)$ being the oscillator strength, then the surface impedance Z has the behavior as shown in (a), in which the real part quickly approaches the air impedance Z_0 above the cutoff Ω_c , whereas the imaginary part decays towards zero. As the imaginary part of Z contributes to the magnitude of reflection only in the form of $|\text{Im}(Z/Z_0)|^2$, its effect on absorption rapidly diminishes beyond Ω_c . In this idealized case the acoustic metamaterial by itself can exhibit a near-perfect absorption spectrum above Ω_c , as shown in (b). Substituting such an absorption spectrum into eqn (1) leads to an inequality $d \geq d_{\min} = 2v_0/(\Omega_c\pi)$. For $\Omega_c/2\pi = 345$ Hz and the absorption spectrum shown in (b), $d_{\min} = 10.25$ cm.

the integrand in eqn (3), rapidly decays to zero for $\omega > \Omega_c$. However, the real part of the impedance is seen to approach the impedance matching condition $Z/Z_0 = 1$ beyond Ω_c . The absorption spectrum can be calculated from eqn (5):

$$A = 1 - \left| \frac{\tanh^{-1}(\Omega_c/\omega)}{\pi - i \tanh^{-1}(\Omega_c/\omega)} \right|^2. \quad (6)$$

This is plotted in Fig. 1b. In this idealized case, just the acoustic metamaterial alone can already achieve near-perfect broadband absorption, requiring only an infinitesimal dissipation coefficient.

Causality constraint and the optimal ϕ for attaining minimum thickness

As the parameter ϕ appears explicitly in $\Omega_{\bar{n}}$, its value is required to realize the optimal design. By substituting $A(\lambda)$ as expressed by eqn (6) into eqn (1), with $\lambda = 2\pi v_0/\omega$ and $B_{\text{eff}} = B_0/\phi$ as noted above, we obtain $d_{\min} = 2v_0/(\phi\Omega_c\pi)$. Since each first order FP resonance frequency is associated with a channel length $\ell_n = \pi v_0/(2\Omega_n)$, it follows from volume conservation of the FP channels that the optimal thickness of the sample, assuming that the longer channels can be folded so as to form a compact volume, is given by $\bar{d} = \sum_{n=1}^N \ell_n/N = [1 - \exp(-2\phi)]\pi v_0/(4\phi\Omega_c)$.

By setting $d_{\min} = \bar{d}$, a value of $\phi_c = 0.832$ is obtained in this particular case. In this manner the causal optimality is explicitly built into the design algorithm to minimize the sample thickness, which is always crucial for comparison between different absorption samples as well as for their practical applications.

It should be noted that in the above, the folding of the channels should not change the front surface area exposed to the incident wave, *i.e.*, the value of ϕ should remain unchanged by channel folding.

The value of ϕ has two separate effects. One is in the determination of $\Omega_{\bar{n}}$ and hence the mode density, which is the most important aspect. Since $\Omega_{\bar{n}}$ depends only on channel length, this aspect is not directly dependent on the actual definition of ϕ as the area fraction of FP channels' cross section. The second effect of ϕ is more directly related to its definition since the fraction of the solid surface, $1 - \phi$, can affect the surface impedance. However, this second aspect can easily be shown to have only a minimal effect on the overall absorption (see Fig. S6 in the ESI†).

It should also be noted that since d_{\min} is evaluated with the target absorption spectrum, the condition of $d_{\min} = \bar{d}$ is also a consistency condition for optimally achieving the target absorption spectrum.

Higher order FP resonances, which become numerous as the frequency increases, can present an adjustment to the initial design. A detailed algorithm, which takes into account all the higher order FP resonances, is presented in the ESI.† The altered mode density, with a distribution that is super-linear in \bar{n} for $\ln \Omega_{\bar{n}}$, can in turn provide an adjusted $\phi_{\text{optimal}} = 0.982$ in the present case. In all the implementations described below, the exact design algorithm was employed. As the actual value of ϕ in our samples is determined by the thickness of the walls separating the FP channels, it is not possible to realize $\phi_{\text{optimal}} = 0.982$ in practice. However, as long as the mode distribution and hence the FP channel lengths are designed in accordance with the ϕ_{optimal} value, the actual value of $\phi = 0.8$ only degrades the absorption result slightly (see Fig. S6 in the ESI†). However, if a value of ϕ differing from ϕ_{optimal} is used in the FP channel length design, then it can be easily shown by simulations that the resulting absorption spectrum would be degraded from the target spectrum.

Metamaterial unit and its characteristics

To implement the designed structure, we let $N = 4 \times 4 = 16$ FP channels compactly arrayed into an acoustic metamaterial in the shape of a cuboid with a square cross section, $L = 2.285$ cm on one side. A single unit is shown in Fig. 2a. Each FP channel has a square cross section that is ~ 4.925 mm on the side, separated from each other with a 0.7 mm thick wall. This implementation gives a value of $\phi = 0.80$, which is smaller than the optimal value. However, the ℓ_n 's are designed in accordance with $\phi_{\text{optimal}} = 0.982$. The position of each channel in the unit is shown in Fig. 2a, where the length of each channel decreases with increasing n . We fold the longer channels in order to obtain a compact structure that can approach \bar{d} . The folding, designed by computer simulations, can be seen for the blue-, pink-, and orange-colored channels as shown in Fig. 2a. In our particular case $\bar{d} = 10.27$ cm, whereas the actual sample has a thickness $d = 10.56$ cm. In Fig. 2b (in red) 14 (of the 16) 1st-order FP resonance frequencies and their oscillator strengths (the highest $\Omega_{16} = 4834 \times 2\pi$ Hz) are shown, with the associated second and third resonances shown in blue and green. The arrangement of

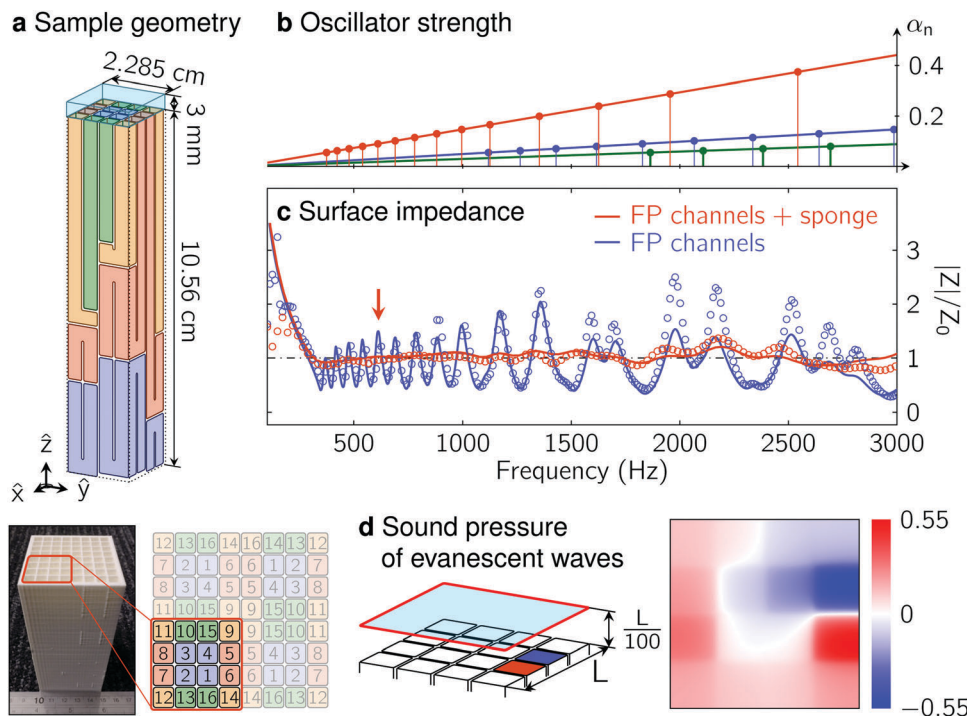


Fig. 2 Metamaterial unit and its features. (a) Schematics of the metamaterial unit consisting of 16 Fabry-Pérot (FP) channels, arrayed in a 4×4 square lattice. The channel's number denotes its order in the sequence of decreasing lengths. Blue channels are coiled by 3 foldings, pink channels are coiled by 2 foldings, orange channels are coiled by 1 folding, and the green channels are straight. The transparent cyan block represents the sponge placed on channels' top surface. A photo image of a sample comprising 4 units arranged in a mirror-symmetric pattern is shown in the lower left panel. (b) The oscillator strength α_n of the FP channels' resonances is plotted as a function of frequency, up to 3000 Hz. The plot shares the same horizontal axis with (c). The red line is for the 1st-order FP resonance, the blue line is for the 2nd-order, and the green line for the 3rd-order. The points indicate the resonant frequencies, designed so that the mode density (including the higher order FP resonances) is inversely proportional to the magnitude of α_n . (c) The surface impedance of the metamaterial unit (blue) and that with 3 mm thick sponge placed on top (red), both plotted as functions of frequency. The circles are deduced from the measured reflection coefficient while the curves are the theory predictions based on eqn (8) and (9). The red arrow denotes the frequency at which the simulations were carried out on the sound pressure field, shown in the right panel below. (d) Right panel: The simulated sound pressure field at 0.22 mm above the front surface of the metamaterial unit at 612 Hz, which is the anti-resonance frequency between the FP resonances of the 5th and 6th channels (blue and red squares), shown on the left panel. The color is indicative of the pressure amplitude normalized to that of the incident wave. At anti-resonance, there is no coupling to the propagating modes; only an evanescent mode exists as explained in the text.

the 16 channels within the metamaterial unit (shown in Fig. 2a) is optimized subject to the geometric requirements of channel folding. Reflection R has been measured by arranging four units (a photo image is shown in Fig. 2a) in a square, placed against a reflecting wall (see the illustration in Fig. 3a). From the measured R the sample impedance $Z/Z_0 = (1 + R)/(1 - R)$ can be deduced. They are shown by the blue circles in Fig. 2c. It can be seen that they oscillate around $Z/Z_0 = 1$. This is expected, since we have only 16 discrete resonances; here the peaks can be associated with the anti-resonances.¹³

By treating each FP channel to be independent from the others, the impedance of the metamaterial unit can be written as

$$Z = \frac{i}{\omega} \left(\frac{1}{16} \sum_{n=1}^{16} g_n \right)^{-1}, \quad (7)$$

in which g_n represents the exact Green function for the FP resonator, $g_n = \phi \tan[\omega l_n \sqrt{(1 + i\beta/\omega)\rho_0/B_0}]/(\omega Z_0)$ (see the ESI[†]), with all the higher order FP modes included. For each resonator, the normal component of the air displacement velocity v_n at the mouth of the n th channel is given by $v_n = -i\omega g_n p$.

It can be easily appreciated that Z should display oscillations as shown by the measured results. However, if a 3 mm layer of acoustic sponge is placed on top of the unit, then the measured impedance is shown by the red circles in Fig. 2c. All the oscillations almost completely vanish. Such behavior was previously observed,⁴⁸ but without the sample thickness or absorption-by-design considerations. The latter are the foci of this work. In particular, it should be noted that without the pre-designed mode density, the flat absorption feature cannot be obtained even with the addition of the sponge; hence design is still the key. Below we show this “absorption valley-filling” effect by the acoustic sponge is due to the surface impedance renormalization effect by the evanescent waves, and their interaction with a highly dissipative medium.

Renormalized impedance from evanescent waves and the dissipation effect

For frequencies that are much less than 15 kHz, we have $L \ll \lambda$. In this regime, not only the angular effect of the incident wave

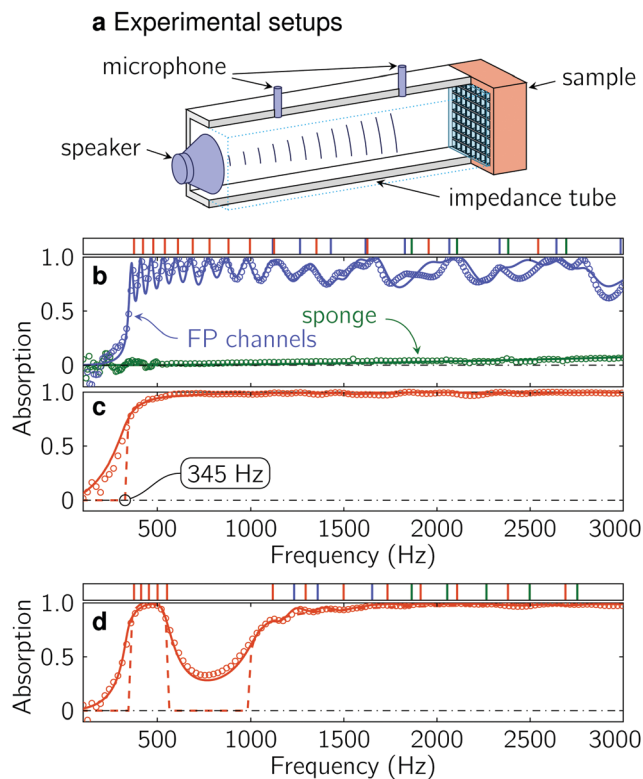


Fig. 3 Experimental realization of designed sound absorbing structures and their characteristics. (a) Schematic illustration for the experimental setups for the impedance tube measurement. (b) The absorption spectrum of the acoustic metamaterial sample (blue circles), and that for a 3 mm sponge backed by a reflecting wall (green circles). The blue and green curves are calculated from theory with the parameter values given in the text. Each of the red lines in the top bar represents a designed 1st-order FP resonance. Each blue line and green line represent, respectively, the 2nd and 3rd order FP resonances. (c) The measured absorption coefficient (circles) of the sample, comprising the designed acoustic metamaterial covered by 3 mm of acoustic sponge, is plotted as a function of frequency. The solid curve is calculated from theory in which the evanescent waves, in interaction with dissipative acoustic sponge, play a major role in filling the valleys in the absorption spectrum seen in (b). For comparison, the spectrum for the idealized case ($N \rightarrow \infty$), Fig. 1, is shown as a dashed line. Near perfect absorption above the designed $\Omega_c = 2\pi \times 345$ Hz can be seen, with excellent agreement between theory and experiment. (d) The measured absorption coefficient (circles) of a sample designed to have a “notch” in the absorption spectrum between 562 and 995 Hz. The sample comprises 16 FP resonators with 3 mm of sponge placed in front. Its absorption behavior outside the notch region is similar to that shown in (c). The solid curve is calculated from theory. For comparison, the absorption spectrum for a continuum of resonances, *i.e.*, $N \rightarrow \infty$ is shown by the dashed line. Different colored lines in the top bar have the same meaning as that shown in (b).

would be minimal, but also the observed impedance of the unit should be the homogenized effective value. At $z = 0$, the unit's surface has inhomogeneous local impedances; hence, the pressure should be expressed as $p(\mathbf{x})$, where $\mathbf{x} = (x, y)$ denotes the lateral coordinate. By writing $p(\mathbf{x}) = \bar{p} + \delta p(\mathbf{x})$, where \bar{p} denotes the value of $p(\mathbf{x})$ averaged over the surface area of the unit and $\delta p(\mathbf{x})$ represents the leftover component; it can be appreciated that the $\delta p(\mathbf{x})$ only couples to the evanescent waves that decay exponentially away from $z = 0$. This is because from

the dispersion relation we have $|\mathbf{k}_\parallel|^2 + \mathbf{k}_\perp^2 = (2\pi/\lambda)^2$; and since the \mathbf{k}_\parallel components from the Fourier transform of $\delta p(\mathbf{x})$ must be larger than $2\pi/\lambda$ (since $L \ll \lambda$), it follows that $\mathbf{k}_\perp^2 < 0$, hence it is evanescent along the z direction. In contrast, the \mathbf{k}_\parallel components of \bar{p} are peaked at $|\mathbf{k}_\parallel| = 0$; hence, \bar{p} couples to the propagating modes. In Fig. 2d, we illustrate the $\delta p(\mathbf{x})$ component at $z = 0.22$ mm and 612 Hz by plotting the full wave simulation results from a normally incident plane wave, carried out by using the commercial package COMSOL. This particular frequency (shown by the red arrow in Fig. 2c) is at the anti-resonance between the 5th and 6th channels' FP resonances, defined as $\bar{p} = 0$ so that there are only evanescent waves.

From the above discussion, we expect the measured impedance to be given by \bar{p}/\bar{v} , where $\bar{v} = \sum_{n=1}^{16} v_n/16$. However, locally we must have $v_n = -i\omega g_n(\bar{p} + \delta p_n)$ with δp_n denoting the value of $\delta p(\mathbf{x})$ at the n th FP channel location. The consideration of evanescent waves implies that eqn (7) should be replaced by a renormalized impedance given by

$$Z^{(e)} = \frac{i}{\omega} \left[\frac{1}{16} \sum_{n=1}^{16} g_n \left(1 + \frac{\delta p_n}{\bar{p}} \right) \right]^{-1}. \quad (8)$$

As derived in the ESI,[†] the lateral interactions between the different FP channels through evanescent waves can be accurately captured by the renormalized Green function $g_n^{(e)}$, which is related to g_n by the Dyson equation with a self-energy term:

$$(g_n^{(e)})^{-1} = g_n^{-1} - \omega^2 \rho_0 (1 + i\beta/\omega) A, \quad (9)$$

so that $Z^{(e)} = i \left(\omega \sum_{n=1}^{16} g_n^{(e)} / 16 \right)^{-1}$. Here $A = 16 \sum_x \sin^2(\alpha_x \pi/4) \sin^2(\alpha_y \pi/4) / (\pi^4 \alpha_x^2 \alpha_y^2 |\mathbf{k}_x|)$ with $|\mathbf{k}_x| = (2\pi/L) \sqrt{\alpha_x^2 + \alpha_y^2}$ for $\alpha_x, \alpha_y = \pm 1, \pm 2, \pm 3, \dots$. The resonance of $g_n^{(e)}$ should occur at a frequency slightly below the resonance of g_n , where $g_n^{-1} = \omega^2 \rho_0 A$ so that $(g_n^{(e)})^{-1} = 0$. In the ESI,[†] this shift is calculated and compared with the experiment, with excellent agreement. In all the calculations, the value $\beta = 11.83$ Hz was used to model the small air dissipation.² The solid blue line as shown in Fig. 2c reflects the excellent agreement between the calculated impedance $Z^{(e)}$ and the measured results.

As can be seen in Fig. 3b, the measured absorption of the metamaterial unit is shown by blue circles. The solid curve is calculated using eqn (8) and (9) to evaluate the $Z^{(e)}$ and the reflection coefficient R , from which $A = 1 - |R|^2$. Except for two frequency ranges, a very good agreement between theory and experiment is seen.

By using the absorption spectrum of the FP channels as shown in Fig. 3b, the integral of the absorption spectrum in eqn (1) yields $d_{\min} = 6.50$ cm $<$ $d = 10.09$ cm, *i.e.*, the metamaterial unit's absorption is sub-optimal in character, owing to the fact that $N = 16$ is not large enough. To achieve the optimal absorption performance with 16 resonators, we added 3 mm of sponge in front of the metamaterial unit. The separately measured absorption of a 3 mm thick sponge is also shown in Fig. 3b by the green circles; the measured result was

modeled by treating the sponge as a uniform medium with a bulk modulus the same as that of air, justified by the fact that the sound predominantly travels through the pores. The fitted sponge mass density is given by $\rho_{\text{sponge}} = [1.4 + i(1420 \text{ Hz})/\omega]\rho_0$. Here the real part, $1.4\rho_0$, can be interpreted as due to the tortuosity of the pores, which lengthens the time of travel and hence an effectively lower sound speed. The imaginary part is two orders of magnitude larger than that for air, due to the small size of the pores and the inevitably larger viscous boundary layer dissipation.² As shown in the ESI† for the combined metamaterial unit plus the 3-mm sponge to be causally optimal, the dissipation coefficient of the sponge has to exceed a critical value of $\beta_c = 946 \text{ Hz}$, which is satisfied in the present case.

The significantly larger imaginary part of the sponge mass density has a dramatic effect on the real part of the impedance. This can be seen from eqn (9) by replacing $\rho_0(1 + i\beta/\omega)$ by ρ_{sponge} . The renormalized resonances become highly damped; consequently, there is a positive real part for $Z^{(e)}$ that is nearly flat as a function of frequency; *i.e.*, the thin layer of a dissipative sponge helped to realize the target absorption spectrum in a very spectacular manner. This can be seen from the red curve in Fig. 2c, which was calculated from eqn (8) and (9).

Broadband near-perfect sound absorbers

In Fig. 3c we show the absorption performance of the combined system, consisting of 3 mm of sponge in front of our designed metamaterial unit. While the designed cutoff frequency is 345 Hz, there is an absorption tail below that. Above the cutoff frequency the absorption reaches 90% at 400 Hz and then increases to an essentially flat, near-perfect absorption all the way to higher frequencies. The agreement between theory and experiment is excellent, up to 3000 Hz. Beyond that, it is shown in the ESI† that the design rule (which includes all the higher order FP resonances) guarantees near-perfect absorption to be maintained, an outcome of FP resonances' equally-spaced frequencies of the higher order modes. The right-hand side of eqn (1) is evaluated to be 10.55 cm, whereas our sample thickness is 10.86 cm. However, if the channel folding can be improved so that the limit of $\bar{d} = 10.27 \text{ cm}$ is reached, then the total thickness would be 10.57 cm, *i.e.*, eqn (1) essentially becomes an equality.

A broadband absorber with strong reflection at a selected frequency band

In comparison to conventional sound absorbing materials, our design strategy can greatly expand the freedom in manipulating the absorption spectrum. As an additional example, shown in Fig. 3d, a metamaterial unit with 16 differently designed FP channels, folded into a 9.03 cm thick cuboid with a 3 mm sponge in front, is shown to open a notch in the absorption spectrum between 562 and 995 Hz, in which $\sim 70\%$ of the sound energy is reflected. Such an absorption spectrum can be

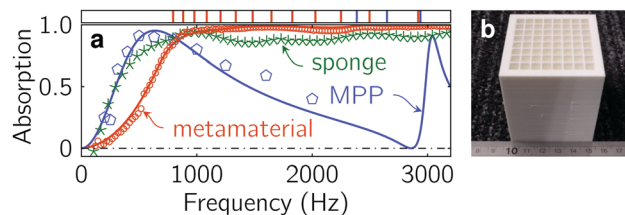


Fig. 4 Absorption comparison between conventional acoustic absorption materials and the designed broadband metamaterial. (a) Comparison of the absorption spectra for the broadband metamaterial unit covered by a 3 mm layer of acoustic sponge, with a total thickness of 5.93 cm (red line denotes theory, red circles denote experiment); the micro-perforated plate (MPP) (blue line denotes theory, blue pentagons denote experiment); and a layer of 6 cm-thick acoustic sponge (green symbols denote measured data). The MPP comprises a 0.2 mm-thick aluminum plate perforated by 0.2 mm diameter circular holes with an area fraction of 2%. The perforated aluminum plate is backed by a 6 cm cavity. The blue curve is evaluated from Maa's theoretical model (eqn (S32) in ESI†), and the experimental data are from Maa's original paper.⁶ The red and blue bars on top of the figure indicate the primary and secondary resonance frequencies of the metamaterial absorber. In the frequency range of $> 900 \text{ Hz}$, the designed metamaterial absorber displays an average of 5 dB less reflection than the acoustic sponge. (b) A photo image of the metamaterial unit with a thickness of 5.63 cm.

useful if wall reflection within the selected frequency band is desired. This sample is noted to be causally optimal as well and has a lower designed value of $\phi_{\text{optimal}} = 0.81$. The contrast between the reflection and absorption bands can be improved by utilizing more resonance channels. The limiting spectrum, with a continuum of resonances and no sponge, is delineated by the dashed line.

Comparison with conventional absorbers

It would be helpful to know how the metamaterial absorber compares with the conventional absorbers, such as the acoustic sponge and MPP. For this purpose, we use samples with the same thickness of 6 cm.

By setting $\Omega_c = 650 \text{ Hz}$, an optimal structure with thickness $d = 5.63 \text{ cm}$ has been fabricated. A photo image of the sample is shown in Fig. 4b. Its absorption performance, with 3 mm of sponge in front (making the total sample thickness 5.93 cm), is shown by the red circles in Fig. 4a. It is very similar to that shown in Fig. 3c, except now the 90% absorption starts at 752 Hz instead of 400 Hz. In the same figure we also plotted, for comparison, the absorption of a layer of 6 cm acoustic sponge supported by a reflecting substrate, as well as the absorption performance of an MPP with a 6 cm-thick back cavity.⁶ It is clear that the three causally optimal structures exhibit absorption behaviors that are very different. But the main point of the comparison is that the somewhat better performances of acoustic sponge and MPP at frequencies lower than 752 Hz are at the expense of higher frequency performance. Within the target frequency range, *i.e.*, $> 900 \text{ Hz}$, the designed metamaterial absorber has been noted to show the best performance.

More details on the comparisons and the MPP are given in Section VI of the ESI.†

Conclusions

We have conceived and implemented a general recipe for fabricating sound absorbing structures that display minimum sample thickness as dictated by the causal nature of the acoustic response function, with a particular realization that can achieve a near-perfect absorption spectrum starting at 400 Hz. Besides the broad application potential of the design strategy that offers tunable absorption spectra, perhaps the most important message of the present work is that metamaterials can be made to function in a true broadband fashion by proper design, aided by the utilization of the synergistic effect presented by evanescent waves, in interaction with a small amount of a highly dissipative medium.

Experimental methods

The designed metamaterial unit was fabricated by using 3D printed polylactide, with fused deposition modeling (FDM) technology. The measurements of the absorption coefficient were performed using the impedance tube method complying with ASTM C384-04(2011) and ASTM E1050-12. As shown in Fig. 3a, a loudspeaker was mounted on one end of the tube, with the absorber mounted on the other end. The impedance tube is 30 cm in length and has a square cross section that is 4.5 cm on each side. Its cross section size implies a cutoff frequency between 3000 and 3500 Hz, beyond which the measured results are inaccurate. Two 1/4-inch condenser microphones (Brüel & Kjær type-4187) were situated at designated positions to sense the amplitude and phase of local pressure modulation. The frequency scan was performed by feeding the sinusoidal signal to a power amplifier and then to the loudspeaker. The outputs of the two microphones were measured using two lock-in amplifiers (Stanford Research SR850) referenced by the same sinusoidal signal. This ensured highly reliable readings of pressure amplitudes and phases at each frequency.

Author contributions

P. S. initiated and supervised the project. M. Y. and P. S. provided a theoretical framework. M. Y. designed the samples and the experiments, and carried out the numerical simulations. S. C. and C. F. carried out the sample fabrication and experiments. M. Y. and P. S. wrote the manuscript.

Competing financial interests

The authors declare no competing financial interests.

Acknowledgements

P. S. wishes to acknowledge Hong Kong Government grants AoE/P-02/12 and ITF UIM292 for the funding support of this research. We thank Songwen Xiao for his help in numerical

simulations, Yan Tan and Xiao Yan for their assistance in sample preparations and testing, and Feng Zhang for his help in sample characterization at the beginning period of this project.

Notes and references

- 1 M. A. Biot, *J. Acoust. Soc. Am.*, 1956, **28**, 168–178.
- 2 J. Allard and N. Atalla, *Propagation of Sound in Porous Media: Modeling Sound Absorbing Materials*, John Wiley & Sons, 2nd edn, 2009.
- 3 Y. Huang, D. Zhou, Y. Xie, J. Yang and J. Kong, *RSC Adv.*, 2014, **4**, 15171.
- 4 X. Jiang, B. Liang, R.-Q. Li, X.-Y. Zou, L.-L. Yin and J.-C. Cheng, *Appl. Phys. Lett.*, 2014, **105**, 243505.
- 5 D.-Y. Maa, *Sci. Sin.*, 1975, **18**, 55–71.
- 6 D.-Y. Maa, *J. Acoust. Soc. Am.*, 1998, **104**, 2861–2866.
- 7 V. M. García-Chocano, S. Cabrera and J. Sánchez-Dehesa, *Appl. Phys. Lett.*, 2012, **101**, 184101.
- 8 Z. Liu, X. Zhang, Y. Mao, Y. Zhu, Z. Yang, C. T. Chan and P. Sheng, *Science*, 2000, **289**, 1734–1736.
- 9 N. Fang, D. Xi, J. Xu, M. Ambati, W. Srituravanich, C. Sun and X. Zhang, *Nat. Mater.*, 2006, **5**, 452–456.
- 10 S. H. Lee, C. M. Park, Y. M. Seo, Z. G. Wang and C. K. Kim, *Phys. Rev. Lett.*, 2010, **104**, 054301.
- 11 Y. Lai, Y. Wu, P. Sheng and Z.-Q. Zhang, *Nat. Mater.*, 2011, **10**, 620–624.
- 12 Y. Wu, Y. Lai and Z.-Q. Zhang, *Phys. Rev. Lett.*, 2011, **107**, 105506.
- 13 M. Yang, G. Ma, Z. Yang and P. Sheng, *Phys. Rev. Lett.*, 2013, **110**, 134301.
- 14 T. Brunet, A. Merlin, B. Mascaró, K. Zimny, J. Leng, O. Poncelet, C. Aristégui and O. Mondain-Monval, *Nat. Mater.*, 2015, **14**, 384–388.
- 15 S. A. Cummer, J. Christensen and A. Alù, *Nat. Rev. Mater.*, 2016, **1**, 16001.
- 16 G. Ma and P. Sheng, *Sci. Adv.*, 2016, **2**, e1501595.
- 17 Y. Xie, W. Wang, H. Chen, A. Konneker, B.-I. Popa and S. A. Cummer, *Nat. Commun.*, 2014, **5**, 5553.
- 18 Y. Li, X. Jiang, B. Liang, J.-C. Cheng and L. Zhang, *Phys. Rev. Appl.*, 2015, **4**, 024003.
- 19 Z. Liang and J. Li, *Phys. Rev. Lett.*, 2012, **108**, 114301.
- 20 Y. Xie, B.-I. Popa, L. Zigoneanu and S. A. Cummer, *Phys. Rev. Lett.*, 2013, **110**, 175501.
- 21 N. Kaina, F. Lemoult, M. Fink and G. Lerosey, *Nature*, 2015, **525**, 77–81.
- 22 J. Li, L. Fok, X. Yin, G. Bartal and X. Zhang, *Nat. Mater.*, 2009, **8**, 931–934.
- 23 J. Zhu, J. Christensen, J. Jung, L. Martin-Moreno, X. Yin, L. Fok, X. Zhang and F. J. Garcia-Vidal, *Nat. Phys.*, 2011, **7**, 52–55.
- 24 J. Christensen and F. J. G. de Abajo, *Phys. Rev. Lett.*, 2012, **108**, 124301.
- 25 L. Zigoneanu, B.-I. Popa and S. A. Cummer, *Nat. Mater.*, 2014, **13**, 352–355.
- 26 C. Faure, O. Richoux, S. Félix and V. Pagneux, *Appl. Phys. Lett.*, 2016, **108**, 064103.
- 27 B. Liang, X. Guo, J. Tu, D. Zhang and J.-C. Cheng, *Nat. Mater.*, 2010, **9**, 989–992.

- 28 R. Fleury, D. L. Sounas, C. F. Sieck, M. R. Haberman and A. Alù, *Science*, 2014, **343**, 516–519.
- 29 J. Mei, G. Ma, M. Yang, Z. Yang, W. Wen and P. Sheng, *Nat. Commun.*, 2012, **3**, 756.
- 30 G. Ma, M. Yang, S. Xiao, Z. Yang and P. Sheng, *Nat. Mater.*, 2014, **13**, 873–878.
- 31 X. Cai, Q. Guo, G. Hu and J. Yang, *Appl. Phys. Lett.*, 2014, **105**, 121901.
- 32 P. Wei, C. Croënne, S. T. Chu and J. Li, *Appl. Phys. Lett.*, 2014, **104**, 121902.
- 33 J. Song, P. Bai, Z. H. Hang and Y. Lai, *New J. Phys.*, 2014, **16**, 033026.
- 34 Y. Duan, J. Luo, G. Wang, Z. H. Hang, B. Hou, J. Li, P. Sheng and Y. Lai, *Sci. Rep.*, 2015, **5**, 12139.
- 35 V. Leroy, A. Strybulevych, M. Lanoy, F. Lemoult, A. Tourin and J. H. Page, *Phys. Rev. B: Condens. Matter Mater. Phys.*, 2015, **91**, 020301.
- 36 M. Yang, C. Meng, C. Fu, Y. Li, Z. Yang and P. Sheng, *Appl. Phys. Lett.*, 2015, **107**, 104104.
- 37 A. Merkel, G. Theocharis, O. Richoux, V. Romero-García and V. Pagneux, *Appl. Phys. Lett.*, 2015, **107**, 244102.
- 38 V. Romero-García, G. Theocharis, O. Richoux, A. Merkel, V. Tournat and V. Pagneux, *Sci. Rep.*, 2016, **6**, 19519.
- 39 Y. Li and B. M. Assouar, *Appl. Phys. Lett.*, 2016, **108**, 063502.
- 40 J. Li, W. Wang, Y. Xie, B.-I. Popa and S. A. Cummer, *Appl. Phys. Lett.*, 2016, **109**, 091908.
- 41 H. Long, Y. Cheng, J. Tao and X. Liu, *Appl. Phys. Lett.*, 2017, **110**, 023502.
- 42 Z. Lu, M. Shrestha and G.-K. Lau, *Appl. Phys. Lett.*, 2017, **110**, 182901.
- 43 V. Achilleos, G. Theocharis, O. Richoux and V. Pagneux, *Phys. Rev. B*, 2017, **95**, 144303.
- 44 L. D. Landau, E. M. Lifshitz and L. P. Pitaevskii, *Electrodynamics of Continuous Media*, Butterworth-Heinemann Ltd, 2nd edn, 1995, ch. 77, vol. 8, p. 265.
- 45 R. M. Fano, *J. Franklin Inst.*, 1950, **249**, 57–83.
- 46 K. N. Rozanov, *IEEE Trans. Antennas Propag.*, 2000, **48**, 1230–1234.
- 47 M. Yang, G. Ma, Y. Wu, Z. Yang and P. Sheng, *Phys. Rev. B: Condens. Matter Mater. Phys.*, 2014, **89**, 064309.
- 48 T. Wu, T. J. Cox and Y. W. Lam, *J. Acoust. Soc. Am.*, 2000, **108**, 643–650.

Supplementary Information for Optimal Sound-Absorbing Structures

Min Yang, Shuyu Chen, Caixing Fu, Ping Sheng

I. Causality constraint on sound absorbing structures

Consider a layer of composite material backed by a rigid reflective wall (Fig. S1a). In response to an incident sound wave, the reflected sound pressure $p_r(t)$ is the superposition of the direct reflection of the incoming sound pressure at that instant, $p_i(t)$ plus those in response to the incoming sound wave at earlier time, $p_i(t-\tau)$, with $\tau > 0$. Hence

$$p_r(t) = \int_0^{\infty} K(\tau) p_i(t-\tau) d\tau, \quad (\text{S1})$$

where $K(\tau)$ is the response kernel in the time domain. By carrying out Fourier transform

$p_{i/r}(\omega) = \int_{-\infty}^{\infty} p_{i/r}(t) e^{i\omega t} dt$, the reflection coefficient for each frequency may be expressed as

$$R(\omega) \equiv \frac{p_r(\omega)}{p_i(\omega)} = \int_0^{\infty} K(\tau) e^{i\omega\tau} d\tau. \quad (\text{S2})$$

From Eq. (S2), $R(\omega)$ is an analytic function of complex ω in the upper half of the complex ω plane. In terms of the wavelength $\lambda = 2\pi v_0 / \omega$, where v_0 is the speed of sounds in air, that means $R(\lambda)$ has no singularities in the lower half-plane of complex λ , but may have zeros that represent total absorptions of incoming energy. Here the imaginary part of λ reflects dissipation.

To determine the constraint on the reflection coefficient $R(\lambda)$ by the causality principle, we introduce an ancillary function $\tilde{R}(\lambda)$ after Fano and Rozanov^{1,2},

$$\tilde{R}(\lambda) \equiv R(\lambda) \prod_n \frac{\lambda - \lambda_n^*}{\lambda - \lambda_n}, \quad (\text{S3})$$

where λ_n , satisfying $R(\lambda_n) = 0$, are the zeros located in the lower half-plane of complex λ , and $*$ stands for complex conjugation. Since \tilde{R} has neither zeros nor poles at $\text{Im}(\lambda) < 0$, $\ln \tilde{R}$ is an analytic function in the lower half-plane of complex λ and the Cauchy theorem is valid, i.e., the integral over a closed contour C in the lower half-plane of complex λ should yield zero, where the contour consists of the real axis of and the semicircle C_{∞} , which belongs to the lower half-plane and has infinite radius as shown in Fig. S1b. Hence

$$\int_C \ln \tilde{R} d\lambda = \int_{-\infty}^{+\infty} \ln \tilde{R} d\lambda + \int_{C_\infty} \ln \tilde{R} d\lambda = 0. \quad (\text{S4})$$

Note that $|\tilde{R}| = |R|$ at real wavelengths and $\ln |R|$ is an even function of λ according to its definition Eq. (S2). Taking the real part of Eq. (S4) yields

$$\text{Re} \int_C \ln \tilde{R} d\lambda = 2 \int_0^\infty \ln |R| d\lambda + \text{Re} \int_{C_\infty} \ln R d\lambda + \text{Re} \sum_n \int_{C_\infty} \ln \frac{\lambda - \lambda_n^*}{\lambda - \lambda_n} d\lambda = 0. \quad (\text{S5})$$

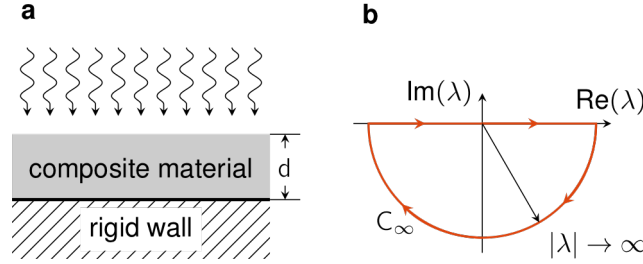


Fig. S1 (a) Schematic for the geometry of composite absorbing layer. (b) The contour for the integral in Eq. (S4).

To calculate the second integral on the right-hand-side of Eq. (S5), we consider the infinite-wavelength limit of R , i.e., the static limit. The reflection from a composite material layer can be characterized by an effective bulk modulus B_{eff} relating to its surface responses³. The surface displacement u under a pressure p is therefore given by the relation (pressure) = (effective bulk modulus) \times (strain), or $u = pd / B_{\text{eff}}$ with d being the sample thickness. The resulting surface impedance is given by $Z = ip / (\omega u) = iZ_0 B_{\text{eff}} \lambda / (2\pi B_0 d)$ with $Z_0 = B_0 / v_0$ being the air impedance and B_0 the bulk modulus of air. Therefore, the reflection coefficient $R = (Z - Z_0) / (Z + Z_0)$ is given by

$$R = \frac{1 + i2\pi dB_0 / (\lambda B_{\text{eff}})}{1 - i2\pi dB_0 / (\lambda B_{\text{eff}})}. \quad (\text{S6})$$

Since $\lim_{|\lambda| \rightarrow \infty} \ln R = i4\pi dB_0 / (\lambda B_{\text{eff}})$, the contour integral is therefore given by

$$\int_{C_\infty} \ln R d\lambda = \lim_{|\lambda| \rightarrow 0} \int_0^{-\pi} i\lambda \ln R d\theta = 4\pi^2 dB_0 / B_{\text{eff}}, \quad (\text{S7})$$

where θ is the argument of complex λ . It should be noted that by taking the limit of $|\lambda| \rightarrow \infty$ in the above contour integral, one is essentially counting all the poles of $\ln R$ in the lower half of the complex λ plane, with the imaginary part of each pole being relevant to the absorption of each resonance of the system. This is evident from the fact that in our previous work³, it has been shown that the static limit the effective bulk modulus $B_{\text{eff}}(\lambda \rightarrow \infty) = \rho_0 d^2 \left(\sum_n \alpha_n / \Omega_n \right)^{-1}$ with Ω_n being the n th resonance

frequency of the system and α_n the relevant oscillator strength defined in the main text. Hence taking the limit of $|\lambda| \rightarrow \infty$ implies all the absorptions related to the resonances of the system are taken into account. In fact, for the designed structures shown in this work, if we let $d = \bar{d}$ as defined in Eq. (S19) below, then the above formula for $B_{\text{eff}}(\lambda \rightarrow \infty)$ is accurately equal to B_0 / ϕ with porosity $\phi \equiv V_{\text{air}} / V_{\text{tot}}$ being the volume fraction of the air phase. This is in agreement with Wood's formula for the composite effective bulk modulus in the static limit, given by $B_{\text{eff}}^{-1} = \phi B_0^{-1} + (1 - \phi) B_{\text{solid}}^{-1}$. Since $B_{\text{solid}} \gg B_0$, $B_{\text{eff}} = B_0 / \phi$ follows. In addition, for samples with identical FP channels either straight or folded, $\phi = \phi = S_{\text{air}} / S_{\text{tot}}$ where S_{air} is the area of FP channels' total surface cross sectional area and S_{tot} being the total area of the sample surface exposed to incident sound. Hence in this work we have $B_{\text{eff}} = B_0 / \phi$.

For the third integral on the right-hand-side of Eq. (S5), since $\lim_{|\lambda| \rightarrow \infty} \ln[(\lambda - \lambda_n^*) / (\lambda - \lambda_n)] = i2\text{Im}(\lambda_n) / \lambda$, we have

$$\int_{C_\infty} \ln \frac{\lambda - \lambda_n^*}{\lambda - \lambda_n} d\lambda = \lim_{|\lambda| \rightarrow \infty} \int_0^{-\pi} i\lambda \ln \frac{\lambda - \lambda_n^*}{\lambda - \lambda_n} d\theta = 2\pi \text{Im}(\lambda_n). \quad (\text{S8})$$

Substitution of Eqs. (S7) and (S8) into Eq. (S5) yields

$$-\int_0^\infty \ln |R(\lambda)| d\lambda = 2\pi^2 d(B_0 / B_{\text{eff}}) + \pi \sum_n \text{Im}(\lambda_n). \quad (\text{S9})$$

As $[1 - A(\lambda)] = |R(\lambda)|^2$, where $A(\lambda)$ stands for the absorption coefficient, and all λ_n are in the lower half-plane, i.e., $\text{Im}(\lambda_n) < 0$, we therefore have the inequality

$$d_{\text{min}} = \frac{1}{4\pi^2} \frac{B_{\text{eff}}}{B_0} \left| \int_0^\infty \ln[1 - A(\lambda)] d\lambda \right| \leq d. \quad (\text{S10})$$

It follows from Eq. (S9) that the equality in (S10) is attained when $R(\lambda)$ has no zeros in the lower half-plane of complex λ . Such $R(\lambda)$ corresponds to the minimum phase-shift frequency dependence^{1,2} for which the variation of the phase of the reflection coefficient with λ does not exceed 2π , in the domain $0 < \lambda < \infty$.

II. Inclusion of higher order FP resonances in the design strategy

In this section we give the derivation of the design algorithm that includes all the higher order FP resonances. For a FP channel with length ℓ_n , its surface impedance is defined at its mouth, $z = 0$, by $Z = p(0) / v(0)$, with

$$p(z) = \cos \left[\omega(z + \ell_n) \sqrt{(1 + i\beta/\omega)\rho_0/B_0} \right],$$

$$v(z) = -i \sin \left[\omega(z + \ell_n) \sqrt{(1 + i\beta/\omega)\rho_0/B_0} \right] / Z_0.$$

For an array of N FP channels with various lengths facing the incident sound wave in parallel, their total impedance is given by

$$Z = iZ_0 \left\{ \phi \sum_{n=1}^N \tan \left[\omega \ell_n \sqrt{(1 + i\beta/\omega)\rho_0/B_0} \right] \right\}^{-1} = i \frac{Z_0 d}{\omega v_0} \left[\sum_{n=1}^N \sum_{m=1}^{\infty} \frac{\alpha_n}{(2m-1)^2 \Omega_n^2 - \omega^2 - i\beta\omega} \right]^{-1}, \quad (\text{S11})$$

where ϕ is the structure's surface porosity (fraction of the total surface area occupied by the open mouths of the FP channels), $\Omega_n = \pi v_0 / (2\ell_n)$ is the 1st-order FP resonance of the n th FP resonator, the terms with $m > 1$ stand for higher order FP resonances, and oscillator strength $\alpha_n = 2d\phi / (\ell_n N) = 4d\phi\Omega_n / (\pi v_0 N)$. It is easy to see that Eq. (S11) is equivalent to Eq. (2) in the main text if we take only the terms with $m = 1$.

In the ideal case, ℓ_n is continuously distributed, i.e., Ω_n is a continuous variable, Eq. (S11) can be converted into an integral:

$$Z \simeq i \lim_{\beta \rightarrow 0} \frac{Z_0 d}{\omega v_0} \left[\int_0^{\infty} \sum_{m=1}^{\infty} \frac{\alpha(\Omega) D(\Omega)}{(2m-1)^2 \Omega^2 - \omega^2 - i\beta\omega} d\Omega \right]^{-1}$$

$$= i \lim_{\beta \rightarrow 0} \frac{Z_0 d}{\omega v_0} \left[\int_0^{\infty} \frac{\sum_{m=1}^{\infty} \alpha(\tilde{\omega}) D(\tilde{\omega}) / (2m-1)}{\tilde{\omega}^2 - \omega^2 - i\omega\beta} d\tilde{\omega} \right]^{-1}, \quad (\text{S12})$$

where $\tilde{\omega} = (2m-1)\Omega$, and $D(\Omega)$ is the modes density of the 1st-order FP resonances. For $\beta \rightarrow 0$, the real part of the integral in Eq. (S12) contributes negligibly, owing to the oscillatory nature of the integrand. The imaginary part of $\lim_{\beta \rightarrow 0} (\tilde{\omega}^2 - \omega^2 - i\beta\omega)^{-1}$ can be accurately approximated by a delta function, hence we have

$$Z(\omega) \simeq \frac{Z_0 d}{\pi\omega v_0} \left[\int_0^{\infty} \sum_{m=1}^{\infty} \frac{\alpha(\tilde{\omega}) D(\tilde{\omega})}{2m-1} \delta(\omega^2 - \tilde{\omega}^2) d\tilde{\omega} \right]^{-1} = \frac{2Z_0 d}{\pi v_0} \left[\sum_{m=1}^{\infty} \frac{\alpha(\Omega) D(\Omega)}{2m-1} \Big|_{\Omega=\omega/(2m-1)} \right]^{-1}. \quad (\text{S13})$$

If we omit the higher order FP resonances and consider only the term $m = 1$, then by recalling that $D(\Omega) = \Delta n / \Delta\Omega$, we have $\Delta\Omega / \Delta n = \pi v_0 \alpha(\Omega) Z(\Omega) / (2Z_0 d)$. Since $\alpha(\Omega) = 4d\phi\Omega / (N\pi v_0)$, we have $\Delta\Omega / \Delta n = (2\phi\Omega / N) [Z(\Omega) / Z_0]$. By letting $\Delta n / N \rightarrow d\bar{n}$ in the limit of $N \rightarrow \infty$, where $\bar{n} = (n-1) / N$, we have thus derived Eq. (4) in the main text.

To include the higher order FP resonances, we recognize that the additional impedances that arise from the higher order resonances are in parallel to that arising from the 1st order FP resonances. Since now we have to deal with multiple impedances even from a single FP resonator, we would like to denote that impedance related to the 1st order FP resonance to be $\tilde{Z}(\Omega)$. In that case

$$\frac{d\Omega}{dn} = \frac{\pi v_0}{2d} \left[\frac{\tilde{Z}(\Omega)}{Z_0} \right] \alpha(\Omega). \quad (\text{S14})$$

Substitution of Eq. (S14) into Eq. (S13) and separating out the term $m=1$ from the m -summation, yields an equation for $\tilde{Z}(\Omega)$,

$$\tilde{Z}(\omega)^{-1} = Z(\omega)^{-1} - \sum_{m=2}^{\infty} \frac{\tilde{Z}(\Omega)^{-1}}{2m-1} \Big|_{\Omega=\omega/(2m-1)}. \quad (\text{S15})$$

The value of \tilde{Z} can be obtained from Eq. (S15) through iterations, based on a given target impedance Z . Simultaneously, Eq. (S15) also expresses the fact that the target impedance at frequency ω is now the consequence of impedance from the 1st order FP resonance, plus the impedance from all the higher order FP resonances, added in parallel.

For example, if the target $Z = Z_0$ for $\omega > \Omega_c$ and divergent for $\omega < \Omega_c$, then the value of \tilde{Z} can be determined in a piecewise fashion as follows. The piecewise fashion of the result is a natural consequence (upon iteration) of the step-function nature of the target impedance. The iteration results show that $Z_0 / \tilde{Z}_1 = 1$ in the first frequency range $\Omega \in [\Omega_c, 3\Omega_c]$, $Z_0 / \tilde{Z}_2 = 2/3$ in the second frequency range $\Omega \in [3\Omega_c, 5\Omega_c]$, $Z_0 / \tilde{Z}_3 = 7/15$ in the third frequency range $\Omega \in [5\Omega_c, 7\Omega_c]$, $Z_0 / \tilde{Z}_4 = 34/105$ in the fourth frequency range $\Omega \in [7\Omega_c, 9\Omega_c]$, $Z_0 / \tilde{Z}_5 = 269/1155$ in the fifth frequency range $\Omega \in [9\Omega_c, 11\Omega_c]$, etc. In each frequency interval i , i.e., for $\Omega \in [(2i-1)\Omega_c, (2i+1)\Omega_c]$, the 1st-order FP resonance frequency distribution can be determined by Eq. (14). That is, with the initial condition $\Omega = (2i-1)\Omega_c$ when the continuous variable $\bar{n} = (n-1)/N = \bar{n}_i = N_i/N$, where N_i denotes the total number of 1st-order FP resonances below $(2i-1)\Omega_c$, Eq. (S14) gives $\Omega_n = (2i-1)\Omega_c \exp[2\phi(\bar{n} - \bar{n}_i)\tilde{Z}_i/Z_0]$. From such 1st order FP resonance frequencies one can easily determine the required lengths of the FP resonators in the design.

In Fig. S2a we plot the natural logarithm of Ω_n as a function of $(n-1)/N$. Here the value of ϕ , needed for the evaluation of Ω_n , is taken to be the causally optimal value determined below. The function $\ln \Omega_n$ versus $(n-1)/N$ is seen to be piecewise hyper-linear. By using this result, discretization of the resonators in the actual design can be easily determined by locating the frequencies

on the vertical axis with the associated (equally-spaced) values of $(n-1)/N$ with N being the total number of FP channels one wants to use. For the broadband absorber presented in the main text with $N = 16$, these frequencies are explicitly indicated by the red dotted lines in Fig. S2a.

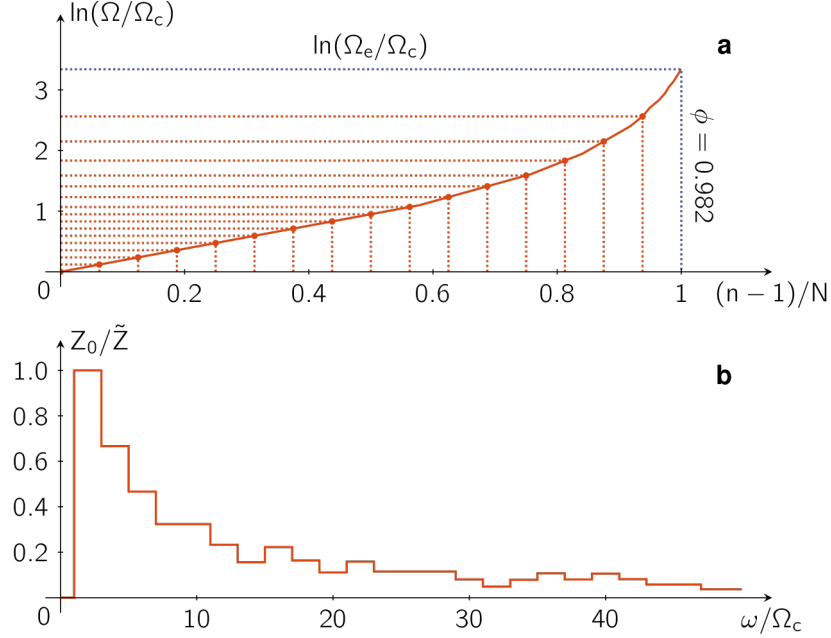


Fig. S2 (a) Natural logarithm of the 1st order FP resonance frequency plotted as a function of the variable $(n-1)/N$ as defined in the text. The discretized frequencies are picked off from the curve with equally-spaced intervals on the horizontal axis. They are indicated by the red dotted lines. (b) The iterated target impedance \tilde{Z} in Eq. (S14) for the 1st-order FP resonances in the broadband absorber design, in which the contributions of higher order FP modes for each channel are taken into account. Here \tilde{Z} is obtained from iterations through Eq. (S15) based on a target impedance that is equals to Z_0 above a cutoff frequency Ω_c and $Z_0/Z = 0$ below the cutoff. The fast decay of Z_0/\tilde{Z} (to zero) guarantees that $Z = Z_0$ can be automatically satisfied by the higher order FP modes if the channels are designed in accordance to the recipe.

One important feature for the sequence Z_0/\tilde{Z}_i is that it decays to zero very quickly (Fig. S2b), i.e., the required 1st-order FP modes density in the high frequency regime is very low. This fact is relevant to the high frequency absorption behavior for the broadband absorber presented in the main text. That is, since $\sum_{m=1}^{\infty} \alpha(\Omega)D(\Omega)/(2m-1)|_{\Omega=\omega/(2m-1)} = 2d/(\pi v_0)$ (this can be easily deduced from Eqs. (S13), (S14), and (S15)), Eq. (S12) can be integrated to yield

$$\frac{Z}{Z_0} = \frac{\pi}{\pi - 2i \tanh^{-1}(\Omega_c / \omega)}. \quad (\text{S16})$$

And the relevant reflection coefficient $R = (Z - Z_0)/(Z + Z_0)$ is given by

$$R = \frac{\tanh^{-1}(\Omega_c / \omega)}{\pi - i \tanh^{-1}(\Omega_c / \omega)}. \quad (\text{S17})$$

That is, at high frequencies the reflection is zero, i.e., the absorption coefficient must approach 1. Therefore, in the broadband absorber design one can use a relatively small number of FP channels, designed for the low frequencies by following the proposed recipe above, and high absorption in the high frequencies regime becomes guaranteed. In particular, this would ensure high absorption above 5000 Hz for the broadband absorber presented in the main text, where there are no measured data.

So far, the parameter ϕ remains un-determined. Below we show that its value should not be arbitrary. Instead, it serves as the critical link between the designed mode density, the sample thickness, and the causal constraint.

In the broadband absorber, the channel length of the FP resonator is given by

$$\ell_n = \frac{\pi v_0}{2\Omega_n} = \pi v_0 \frac{\exp[2\phi(\bar{n}_i - \bar{n})\tilde{Z}_i / Z_0]}{2(2i-1)\Omega_c}, \quad (\text{S18})$$

provided its 1st-order resonance is located in the frequency range $\Omega \in [(2i-1)\Omega_c, (2i+1)\Omega_c]$. Since the channel length can vary, we wish to know the minimum thickness of the sample by optimally folding the FP channels, without changing the overall area exposed to the incident wave. This minimum thickness \bar{d} can be obtained through volume conservation of the FP channels. Here we evaluate \bar{d} by focusing on only the air channels of the FP resonators. Since the FP channels' cross sections occupy a fraction ϕ of the surface area, \bar{d} is given by

$$\bar{d} = \lim_{N \rightarrow \infty} \sum_{n=1}^N \frac{\ell_n}{N} = \pi v_0 \lim_{N \rightarrow \infty} \int_{\Omega_c}^{\Omega_c(\phi)} \frac{1}{\Omega} \frac{dn}{d\Omega} d\Omega / (2N), \quad (\text{S19})$$

where the upper limit of the integral, $\Omega_c(\phi) = \lim_{N \rightarrow \infty} \Omega(n = N, \phi)$, is determined by the total number of 1st order mode number N , which is equal to the FP channel number. The numerical evaluation of Eq. (S19), with $N=16$, gives $\bar{d} = [0.6395 - 859.74 \exp(-12.82\phi)]v_0 / (\phi\Omega_c)$. By requiring $\bar{d} = d_{\min} = 2v_0 / (\phi\Omega_c\pi)$ given in the main text, we obtain the causally optimal value $\phi_{\text{optimal}} = 0.982$, with the upper limit $\Omega_c = 28.4\Omega_c$ (indicated in Fig. S2a by the blue dotted line). Since in experimental implementation the value of ϕ is determined by the wall thickness in our design, such a high value of ϕ_{optimal} is not realizable in practice. However, a lower value of the actual ϕ is seen to only degrade the absorption somewhat, as long as the mode distribution (and hence the length of the channels) is designed in accordance with the ideal value ϕ_{optimal} . The degradation effect can be seen in Fig. S6, where the designed sample has a lower surface coverage $\phi = 0.8$, leading to a degradation of reflection from its ideal value by about 5 dB, even though the actual value of the absorption coefficient is still in the range of 97-99%.

As another example, other than the broadband absorber presented in the main text, we have also considered a target absorption spectrum which starts with near-perfect absorption from 345 Hz and has a notch in the frequency interval [562 Hz, 995 Hz] where the absorption is close to zero. The target impedance is given by $Z(\omega) = Z_0[2 - A(\omega) + 2\sqrt{1 - A(\omega)}] / A(\omega)$. Based on this target impedance the impedance $\tilde{Z}(\omega)$ can be obtained from Eq. (S15) through iterations. Substitution of \tilde{Z} into Eq. (S14) gives the designed resonance frequencies $\Omega_n(N, \phi)$ as a function of total channel number N and the parameter ϕ . The associated FP channel length ℓ_n can then be determined. The minimum thickness of the absorber, $d_{\min} = 8.73$ cm, is determined from the casual integral (S10) of the absorption spectrum shown by the dashed line in Fig. 3c in the main text, which is based on the integral of Eq. (S12) with $N \rightarrow \infty$. In this case the value $\phi_{\text{optimal}} = 0.81$ is determined from $d_{\min} = \bar{d} = \lim_{N \rightarrow \infty} \sum_{n=1}^N \ell_n / N$. The experimentally measured absorption for this design, with $N = 16$, is presented in the main text as Fig. 3c. Here $\bar{d} = 8.85$ cm, and the real sample thickness is 9.03 cm due to the non-ideal folding of the channels. The result shown in Fig. 3c in the main text has a 3-mm layer of sponge placed in front; hence the total thickness of the sample is 9.33 cm.

III. Derivation of self-energy due to cross-channel coupling by evanescent waves

Since the surface impedance of the metamaterial unit is laterally inhomogeneous, it follows that the sound pressure field $p(\mathbf{x})$, where \mathbf{x} denotes the lateral coordinate at the plane $z = 0$, must necessarily be inhomogeneous as well. By decomposing the pressure field as $p(\mathbf{x}) = \bar{p} + \delta p(\mathbf{x})$, where \bar{p} is the surface-averaged value, it has been shown in the main text that $\delta p(\mathbf{x})$ is only coupled to the evanescent waves that decay exponential away from $z = 0$. In contrast, \bar{p} couples to the far-field propagating modes. Therefore, the measured surface impedance should be given by $Z = \bar{p} / \bar{v}$ with $\bar{v} = d\bar{u} / dt$ being the surface-averaged z component of the air displacement velocity. Reflection coefficient is given by $R = (Z - Z_0) / (Z + Z_0)$.

We expand $\delta p(\mathbf{x})$ in terms of the normalized Fourier basis function $f_{\alpha}(\mathbf{x}) = \exp[i\mathbf{k}_{\alpha} \cdot \mathbf{x}] / L$, where $\alpha = (\alpha_x, \alpha_y)$ is discretized by the condition that the area integral of f_{α} over the surface of the metamaterial unit must vanish, due to the fact that the same condition applies to $\delta p(\mathbf{x})$. That means

$$|\mathbf{k}_{\alpha}| = (2\pi / L) \sqrt{\alpha_x^2 + \alpha_y^2}, \text{ with } \alpha_x, \alpha_y = \pm 1, \pm 2, \dots$$

$$\delta p(\mathbf{x}, z) = \sum_{\alpha} \delta p_{\alpha} f_{\alpha}(\mathbf{x}) e^{-\sqrt{k_{\alpha}^2 - k_0^2} z}, \quad (\text{S20})$$

where δp_α denotes the expansion coefficient, and $k_0 = 2\pi/\lambda$. The exponential variation of $\delta p(\mathbf{x}, z)$ means that it can couple to the z component of the air displacement velocity through Newton's law, $\partial \delta p / \partial z = -i\omega\rho_0\delta v$, so that

$$\delta v(\mathbf{x}) = \delta v(\mathbf{x}, z=0) = \frac{-i}{\omega\rho_0} \sum_{\alpha} \delta p_{\alpha} \sqrt{|\mathbf{k}_{\alpha}|^2 - k_0^2} f_{\alpha}(\mathbf{x}). \quad (\text{S21})$$

By multiplying both sides of Eq. (S21) by $f_{\alpha}^*(\mathbf{x})$ and integrating over the surface of the metamaterial unit's surface, we can solve for δp_{α} :

$$\delta p_{\alpha} = i\omega\rho_0 \frac{\int_{\text{surface}} v(\mathbf{x}) f_{\alpha}^*(\mathbf{x}) d\mathbf{x}}{\sqrt{|\mathbf{k}_{\alpha}|^2 - k_0^2}}, \quad (\text{S22})$$

where $v(\mathbf{x}) = \bar{v} + \delta v(\mathbf{x})$. It should be noted that in the above, the integral of $v(\mathbf{x}) f_{\alpha}^*(\mathbf{x})$ is the same as the integral of $\delta v(\mathbf{x}) f_{\alpha}^*(\mathbf{x})$, since the integral of $\bar{v} f_{\alpha}^*(\mathbf{x})$ is zero. By substituting Eq. (S22) into Eq. (S20) and then interchanging the order of summation and integration, we obtain

$$\delta p(\mathbf{x}) = \delta p(\mathbf{x}, z=0) = i\omega\rho_0 \int_{\text{surface}} \Lambda(\mathbf{x}, \mathbf{x}') v(\mathbf{x}') d\mathbf{x}', \quad (\text{S23})$$

where $\Lambda(\mathbf{x}, \mathbf{x}') \equiv \sum_{\alpha} f_{\alpha}^*(\mathbf{x}') f_{\alpha}(\mathbf{x}) / \sqrt{|\mathbf{k}_{\alpha}|^2 - k_0^2}$. Since $|\mathbf{k}_{\alpha}| \gg k_0$, we can approximate $\sqrt{|\mathbf{k}_{\alpha}|^2 - k_0^2}$ by $|\mathbf{k}_{\alpha}|$. By discretizing the 2D coordinate \mathbf{x} by its 16 values, \mathbf{x}_n , that denotes the center position of the n th FP channel, and replacing $d\mathbf{x}'$ by $L^2/16$ and the integral by summation, we have:

$$\delta p_n = i\omega\rho_0 \sum_{m=1}^{16} \Lambda_{nm} v_m, \quad (\text{S24})$$

$$\begin{aligned} \Lambda_{nm} &= \frac{16 \int_{\sigma_n} f_{\alpha}(\mathbf{x}) d\mathbf{x} \int_{\sigma_m} f_{\alpha}^*(\mathbf{x}') d\mathbf{x}'}{L^2 |\mathbf{k}_{\alpha}|} \\ &= 16 \sum_{\alpha} \frac{\sin^2(\alpha_x \pi/4) \sin^2(\alpha_y \pi/4)}{\pi^4 \alpha_x^2 \alpha_y^2 |\mathbf{k}_{\alpha}|} \exp[i\mathbf{k}_{\alpha} \cdot (\mathbf{x}_m - \mathbf{x}_n)], \end{aligned} \quad (\text{S25})$$

where σ_n denotes the cross-sectional area of the n^{th} FP channel, and $v_m = v(\mathbf{x}_m)$, $\delta p_n = \delta p(\mathbf{x}_n)$.

According to the definition of Green function, at the mouth of the n th FP channel, we have

$$v_n = -i\omega g_n (\bar{p} + \delta p_n). \quad (\text{S26})$$

Substitution of Eq. (S24) into Eq. (S26) gives

$$\begin{aligned}
v_n &= -i\omega \left(g_n + \omega^2 \rho_0 \sum_m g_n \Lambda_{nm} g_m + \dots \right) \bar{p} \\
&= -i\omega \left[\left(g_n + \omega^2 \rho_0 g_n^2 \Lambda_{nn} + \omega^4 \rho_0^2 g_n^3 \Lambda_{nn}^2 + \dots \right) + \omega^2 \rho_0 \sum_{m \neq n} g_n \Lambda_{nm} g_m + \dots \right] \bar{p} \\
&= -i\omega \left(\frac{g_n}{1 - \omega^2 \rho_0 g_n \Lambda_{nn}} + \sum_m \Pi_{nm} \right) \bar{p}. \tag{S27}
\end{aligned}$$

We have rearranged the series by separating the terms involving only Λ_{nn} , since $\Lambda_{nn} \gg \Lambda_{nm} (m \neq n)$ by orders of magnitude. Numerically, the last term in the bracket is also small and hence only constitutes small adjustment to the results. According to the Eq. (8) in the main text, the renormalized impedance is given by $Z^{(e)} = 16 \bar{p} / \sum_{n=1}^{16} v_n$. Substitution of Eq. (S27) (with the $\sum_m \Pi_{nm}$ term neglected) into this expression for $Z^{(e)}$ gives

$$Z^{(e)} = i \left(\frac{\omega}{16} \sum_{n=1}^{16} g_n^{(e)} \right)^{-1}, \tag{S28}$$

where the effective Green function can be expressed in the form of the Dyson equation with a self-energy term:

$$\left(g_n^{(e)} \right)^{-1} = g_n^{-1} - \omega^2 \rho_0 \Lambda. \tag{S29}$$

Here $\Lambda \equiv \Lambda_{nn}$. Below we show this self-energy can predict the resonance frequency shifts of the FP resonators.

IV. Shift of the resonance frequencies due to the renormalization effect by evanescent waves

The exact Green function for a single FP channel with length ℓ_n , $g = i / (\omega Z)$, can be derived from Eq. (S11) as

$$g_n = \frac{\phi}{\omega Z_0} \tan \left[\omega \ell_n \sqrt{(1 + i\beta / \omega) \rho_0 / B_0} \right]. \tag{S30}$$

Here the coefficient $\beta = 14.2$ Hz is an effective parameter characterizing air's viscosity in FP channels. Its value is obtained by fitting the experimental data.

The renormalized impedance $Z^{(e)}$ of the FP resonators array can then be obtained by substituting Eq. (S30) into Eqs. (S27) and (S28). Since the resonance modes are best detected by the imaginary part of the Green function, which in the present case is given by $\text{Im}(G) = \text{Im} \left[i / (\omega Z^{(e)}) \right]$, we have plotted the dimensionless quantity $\text{Im}(G) \Omega_c Z_0$ in Fig. S3. Here $\Omega_c = 2\pi \times 345$ Hz is the cutoff frequency.

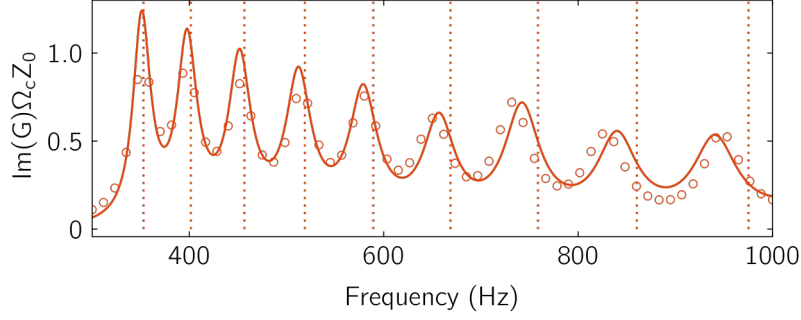


Fig. S3 The imaginary part of the Green function for the metamaterial unit, plotted as a function of frequency. The metamaterial unit consists of 16 FP channels in a 4×4 square lattice, shown in Fig. 2a of the main text. Here the solid curve is the prediction from the theory including the evanescent waves and the viscosity of air. The open circles are results deduced from experimental reflection measurements, where we have used the formula $\text{Im}(G)\Omega_c Z_0 = \text{Im}\left\{-i\Omega_c(R-1)/[\omega(R+1)]\right\}$. It is seen that the peak positions, which indicate the renormalized resonances, are all down-shifted from the dotted lines that mark the original FP resonance frequencies (Ω_n 's). Excellent theory-experiment agreement is seen.

As shown in Fig. S3, for the metamaterial unit the theoretically predicted positions of the newly emerged resonances (solid curve) fit the experiment (open circles) very well, and they all have a clear downward shift from the original FP resonances, $\Omega_n = \pi v_0 / (2\ell_n)$, denoted by the vertical dotted lines. Physically, the downshift can be understood as due to the extra air mass participating in the resonant motion at the mouth of the FP channel, arising from the evanescent waves.

V. Critical dissipation for casual optimality

In the main text, the causal optimality of the 16-units broadband absorber is achieved by placing a layer of 3 mm acoustic sponge in front of it. Here we discuss the property requirement for the sponge. The description of sponge's properties $\rho_{\text{eff}} = \rho_0[1.4 + i(1420 \text{ Hz})/\omega]$ is a simplified form for the effective medium theory of porous medium that assumes the solid skeleton of sponge to be rigid while sounds propagates in the pores. Adapted from Ref [5], according to the model of Johnson et al.⁶, $\rho_{\text{eff}} = \rho_0\alpha(\omega)$ with $\alpha(\omega)$ being the dynamic tortuosity, given by

$$\alpha(\omega) = \alpha_\infty + \frac{i\eta_0\varphi}{\omega\rho_0\kappa_0} \sqrt{1 - \frac{i\omega\rho_0}{\eta_0} \left(\frac{2\alpha_\infty\kappa_0}{\Lambda_v\varphi} \right)^2}. \quad (\text{S31})$$

Here, α_∞ is the tortuosity of a porous medium that is 1.4 in our case, η_0 is the viscosity of air, φ is the sponge porosity, and κ_0 is its static permeability. $\Lambda_v = 2 \int_{V_f} v_{\text{inviscid}}^2 dV / \int_{S_f} v_{\text{inviscid}}^2 dS$ is the viscous characteristic length with v_{inviscid} being the air velocity field in the absence of viscosity, and the two integrals are carried on the volume of pores and the surface of solid skeleton, separately. If the

frequency is not very high, $\alpha(\omega)$ can be approximated by $\alpha_\infty + i\beta/\omega$ with $\beta = \eta_0\phi/(\rho_0\kappa_0)$. And the dissipation property for a sponge is sensitive to the ratio between its porosity and static permeability.

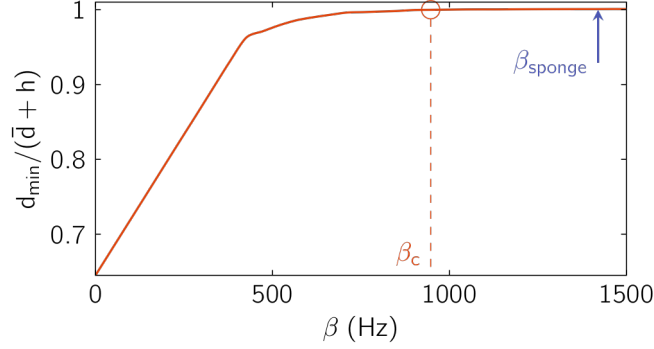


Fig. S4 The minimum thickness d_{\min} of the broadband absorber in the main text, with $h = 3$ mm sponge in front, as dictated by the casual integral, Eq. (S10), in which the absorption spectrum is that predicted by the renormalized impedance $Z^{(e)}$ in Eqs. (S27) and (S28) with ρ_0 replaced by ρ_{spong} . Here the dissipation coefficient β for the front sponge has been treated as a variable. It is seen that there is a critical value $\beta_c = 946$ Hz above which the causal optimality (defined as $d_{\min} = d$) is attained. The blue arrow denotes the dissipation of the sponge used in the experiment.

In order for the addition of 3 mm sponge to the acoustic metamaterial unit to achieve causal optimality, we have calculated the casual integral, Eq. (S10), for absorption spectra with different sponge cover characterized by different values of β . The results are shown in Fig. S4, where the vertical axis is the ratio of d_{\min} divided by the total thickness of the sample. Here $h=3$ mm is the sponge thickness, and \bar{d} is the minimum thickness of the cuboid sample achievable by perfect folding of the longer FP channels. The value of $d_{\min}/(\bar{d} + h) = 1$ indicates causal optimality. In Fig. S4 this ratio, with d_{\min} calculated by Eq. (S10), is plotted as a function of β . It is seen that there is the existence of a critical $\beta_c = 946$ Hz. For those sponges with $\beta < \beta_c$, causal optimality cannot be satisfied. However, the acoustic sponge used in our sample is safely in the range of $\beta > \beta_c$.

VI. Comparison with conventional acoustic materials

In this section, we compare our metamaterial absorber with the conventional acoustic absorption materials, the micro-perforated panel (MPP) absorber and acoustic sponge. Owing to measurement accuracy, we choose to compare our 6-cm absorption structure with similar thickness MPP absorber and acoustic sponge.

The MPP absorber⁴ and acoustic sponge are two very effective sound absorbers. However, the MPP has proven to be excellent only at multiple distinct frequencies, and such an absorption spectrum

can also achieve causal optimality, provided the MPP's perforated hole diameter is small enough (see Fig. S5b).

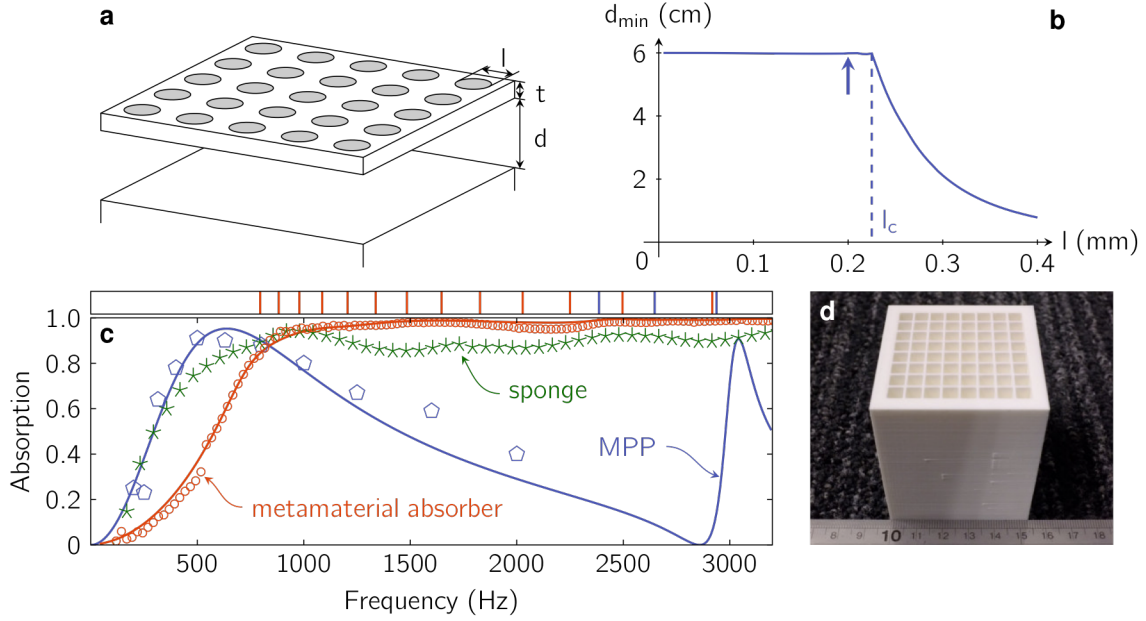


Fig. S5 (a) A schematic drawing for the MPP absorber. (b) The minimal thickness d_{\min} determined by the causal integral of the absorption spectrum, Eq. (S10), for a MPP with perforation diameter l , panel thickness $t = 0.2$ mm, lattice constant $b = 2.5$ mm, and back chamber depth $d = 6$ cm. The blue arrow indicates the perforation's diameter of $l = 0.2$ mm, whose relevant absorption spectrum (blue line and symbols) is shown in (c). (c) Comparison of the absorption spectra for the MPP (blue line (theory) and symbols (experiment)) with $l = 0.2$ mm and a total thickness of ~ 6 cm; the broadband metamaterial unit covered by a 3-mm layer of acoustic sponge, with a total thickness of 5.93 cm (red line (theory) and symbols (experiment)), and a layer of 6 cm-thick acoustic sponge (green symbols (measured data)). The blue curve is from Maa's theoretical model Eq. (S32), and the pentagons are the experimental data from Maa's original paper (4). (d) A photo image of the metamaterial unit with a thickness of 5.63 cm. With the addition of 3 mm of acoustic sponge in front, the absorber has a total thickness similar to the MPP.

As shown in Fig. S5a, consider a panel that is $t = 0.2$ mm thick, with perforated holes that are arranged in a square lattice with a lattice constant $b = 2.5$ mm. The panel is backed by a chamber with $d = 6$ cm⁴. Maa's theoretical model⁴ has proven to be very accurate for characterizing MPP's absorption. For uniform circular perforations with diameter l the absorption is given by⁴

$$A(\omega) = \frac{4r}{(1+r)^2 + [\omega m - \cot(\omega d / v_0)]^2}. \quad (\text{S32})$$

Here,

$$r = \frac{32\eta_0 t}{\sigma \rho_0 v_0 l} k_r, \quad k_r = \left[1 + \frac{k^2}{32}\right]^{1/2} + \frac{\sqrt{2}}{32} k \frac{l}{t},$$

$$m = \frac{t}{\sigma v_0} k_m, \quad k_m = 1 + \left[1 + \frac{k^2}{2}\right]^{-1/2} + 0.85 \frac{l}{t},$$

and

$$k = l\sqrt{\omega\rho_0 / (4\eta_0)}, \quad \sigma = l^2\pi / (4b^2),$$

where the quantity $\sqrt{\eta_0 / (\omega\rho_0)}$ is usually denoted the viscous boundary layer thickness. Here η_0 is related to the effective air dissipation parameter β in the main text, through the solution of the sound wave propagation in the FP channel.

In Fig. S5c, the solid blue line is the theory prediction of the MPP absorption with the parameter values given above, and $l = 0.2$ mm. The open circles are the experimental results⁴. The causal integral, Eq. (S10), gives $d_{\min} \simeq d = 6$ cm, i.e., causal optimality is satisfied. In Fig. S5b, we plot the d_{\min} calculated from the predicted absorption spectra. It turns out that a critical perforation diameter $l_c \simeq 0.025$ mm exists, and for $l > l_c$ causal optimality is not satisfied. It is somewhat surprising that the critical value of the perforation hole diameter agrees so well with the “best” diameter of the holes as determined from an entirely different perspective⁴.

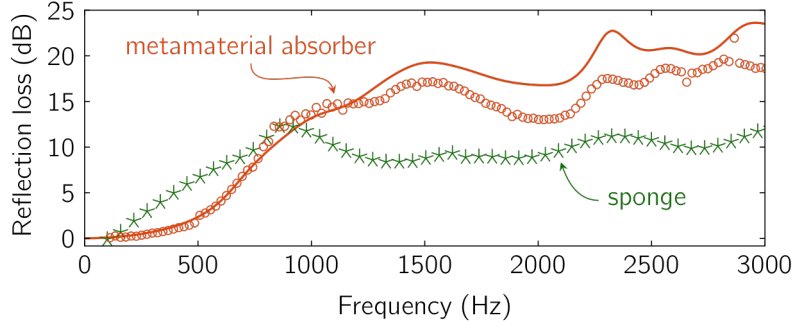


Fig. S6 Reflection loss (dB) comparison for the 6 cm thick acoustic sponge and 5.93 cm thick metamaterial absorber shown in Fig. S5c. The red curve represents the theory prediction of our metamaterial absorber, and the open circles are from experiment. The poorer experimental absorption can be attributed to the lower achievable value of $\phi = 0.8$ as compared to its optimal value ϕ_{optimal} . Its effect can be easily assessed by the formula $A = 1 - [(Z/Z_0 - 1)/(Z/Z_0 + 1)]^2$. If Z/Z_0 is 20% larger than $Z/Z_0 = 1$, i.e., $Z/Z_0 \simeq 1.2$ as expected by the lower value of $\phi = 0.8$, then the absorption would be lowered by 0.8%. The green stars are the experimentally measured data of acoustic sponge. To reach the absorption level of our design structure within the target range, the sponge thickness would need to be increased by at least 50%. If thin walls can be realized technically so that the theory prediction can be realized, then the advantage of the metamaterial absorber in the target frequency range (solid line) is seen to be quite substantial.

To compare with the particular MPP absorber whose absorption spectrum is shown in Fig. S5c, we have redesigned our broadband metamaterial absorber by setting the cutoff frequency $\Omega_c = 650$ Hz, and folded the 16 FP channels into a 5.63 cm thick cuboid. The value of $\phi = 0.8$ for the sample is the same as that for the broadband absorber presented in the main text, even though the FP channels were designed with $\phi_{\text{optimal}} = 0.982$. A photo image of the sample is shown in Fig. S5d. Four of such units

were arranged into a square with the cross section that fits the cross section of the impedance tube (see Fig. S5d). The metamaterial unit was covered by a layer of 3 mm thick acoustic sponge, so that the total thickness of the absorber, 5.93 cm, is similar to that of the MPP in Maa's work⁴. The absorption spectrum of this metamaterial absorber is shown in Fig. S5c (red symbols for the experiment, red line the theory prediction). It is seen that near-perfect flat absorption starts around 752 Hz. The causal integral of this spectrum gives $d_{\min} = 5.86$ cm, very close to the actual thickness of the sample. In the same figure, we also compared the absorption of a layer of 6 cm sponge with rigid substrate. The sponge absorption coefficient is noted to be also causally optimal. It is clear that the three causally optimal structures exhibit absorption behaviors that are very different. The MPP starts its maximum absorption at a lower frequency, ~ 640 Hz, but quickly drops to nearly zero before its next resonance. And although the sponge exhibits a broadband absorption, it trades off poorer performance in higher frequencies as compared to the designed metamaterial absorber, against a somewhat better absorption at lower frequencies. This comparison emphasizes the fact that, in the causal inequality, low frequency behavior dominates the contribution to the sample thickness. Here, the somewhat better low frequency absorption of the MPP or sponge is at the cost of degrading the absorption over large ranges of higher frequencies. The novelty of our approach lies in making the absorption spectrum tunable, while integrating the causal optimality as part of the design.

In engineering practice, decibel (dB) is a more relevant unit. In Fig. S6 we compare the absorption by 6 cm of sponge against that by the 5.93 cm thick metamaterial, by their reflection loss characterized in decibels. It is seen from Fig. S6 that in the target frequency regime, i.e., above 800 Hz, our metamaterial absorber has an advantage of ~ 5 to 10 dB in reducing the reflection through absorption. To reach the same level of absorption within the target frequency range, the sponge thickness needs to be increased by a factor of at least 50%. If the thin walls can be technically realized in our metamaterial unit, then the advantage over conventional absorbers can be fairly substantial within the target range, i.e, between 10-15 dB if the solid red line is used for comparison in Fig. S6.

References

1. R. M. Fano. *J. Franklin Inst.*, 1950, **249**, 57–83.
2. K. N. Rozanov. *IEEE Trans. Antennas. Propag.*, 2000, **48**, 1230–1234.
3. M. Yang, G. Ma, Y. Wu, Z. Yang, P. Sheng. *Phys. Rev. B*, 2014, **89**, 064309.
4. D-Y. Maa. *J. Acoust. Soc. Am*, 1998, **104**, 2861–2866.
5. J. Allard and N. Atalla. *Propagation of Sound in Porous Media: Modeling Sound Absorbing Materials*. 2nd Edition (John Wiley & Sons, 2009).
6. D. L. Johnson, J. Koplik, R. Dashen. *J. Fluid Mech*, 1987, **176**, 379–402.